Aerosol and Air Quality Research, 19: 657–670, 2019

ISSN: 1680-8584 print / 2071-1409 online
doi: 10.4209/aaqr.2018.01.0010

Atmospheric CO_2 and $\delta^{13}C$ Measurements from 2012 to 2014 at the Environmental Research Station Schneefernerhaus, Germany: Technical Corrections, Temporal Variations and Trajectory Clustering

Homa Ghasemifard[1*], Ye Yuan[1], Marvin Luepke[1], Christian Schunk[1], Jia Chen[2,3], Ludwig Ries[4], Michael Leuchner[1†], Annette Menzel[1,3]

[1] *Professorship of Ecoclimatology, Technische Universität München, 85354 Freising, Germany*
[2] *Professorship of Environmental Sensing and Modeling, Technische Universität München, 80333 Munich, Germany*
[3] *Institute for Advanced Study, Technische Universität München, 85748 Garching, Germany*
[4] *German Environment Agency (UBA), 82475 Zugspitze, Germany*

ABSTRACT

This study presents continuous atmospheric CO_2 and $\delta^{13}C$ measurements by wavelength-scanned cavity ring down spectroscopy (Picarro G1101-i) at the high-mountain station Schneefernerhaus, Germany. $\delta^{13}C$ values were post-corrected for methane and water spectral interferences using accompanying measurements of CH_4 and H_2O, and CO_2 in dried air, respectively. The best precision of ±0.2‰ for $\delta^{13}C$ and of ±4 ppb for CO_2 was obtained with an integration time of about 1 hour for $\delta^{13}C$ and 2 hours for CO_2. The seasonality of CO_2 and $\delta^{13}C$ was studied by fitting background curves for a complete 2-year period. Peak-to-peak amplitudes of the averaged seasonal cycle were 15.5 ± 0.15 ppm for CO_2 and 1.97 ± 0.53‰ for $\delta^{13}C$, respectively. Based on the HYSPLIT Model, air masses were classified into five clusters, with westerly and northeasterly flows being the most and the least frequent, respectively. In the wintertime, northwest and northeast clusters had a higher median level for ΔCO_2 and a lower median level for $\Delta\delta^{13}C$ (the difference between observed and background concentrations), likely caused by anthropogenic emissions. In the summertime, air masses from the northwest had the lowest ΔCO_2 and the highest $\Delta\delta^{13}C$. Potential source contribution functions (PSCFs) were used to identify the potential source and sink areas. In winter, source areas for high CO_2 mixing ratios (> 75th percentile) were mainly located in northwestern Europe. In summer, areas with high $\delta^{13}C$ ratios (> 75th percentile), indicating a carbon sink, were observed in the air from Eastern and Central Poland.

Keywords: CO_2 mixing ratio; $\delta^{13}C$; Mountain station; Trajectory HYSPLIT; PSCF.

INTRODUCTION

The sources and sinks of atmospheric carbon dioxide (CO_2) play a critical role in governing global climate. Human activities, especially fossil fuel combustion, cement manufacturing and land use changes trigger anthropogenic emissions and thus contribute to a steady increase of the atmospheric CO_2 mixing ratio (IPCC, 2014; WMO, 2016; Xu *et al.*, 2017). Nearly half of the emitted CO_2 is taken up by both the terrestrial biosphere and absorption in the ocean reservoirs with a similar share each (Le Quéré *et al.*, 2016). The atmosphere and these two major sinks are linked via the balance between photosynthesis, respiration fluxes and CO_2 dissolving in ocean water (Ciais *et al.*, 2013). Considering the risk of the ocean sink to become saturated, the risk of the biosphere sink to turn into a source and of a consequential rapid increase in atmospheric CO_2 growth rates, it is crucial to monitor atmospheric CO_2 mixing ratio continuously with high temporal resolution in order to identify the source and sink contributions (Cramer *et al.*, 2001; IPCC, 2013).

The stable carbon isotope composition of CO_2 ($\delta^{13}C$) allows distinguishing the exchange of fossil carbon from the atmosphere and surface reservoir fluxes (Keeling *et al.*, 2011). During photosynthesis, most plants of the terrestrial biosphere prefer to take up the light isotopologue $^{12}CO_2$ and thus discriminate against $^{13}CO_2$ (~18‰) (Farquhar *et al.*, 1989). In contrast, during oceanic uptake of CO_2, there is almost no discrimination (~2‰) (Mook *et al.*, 1974). Since the discrimination by oceans is small, the carbon

† Now at Springer Nature B.V., Dordrecht, 3311 GX, Netherlands

* Corresponding author.
Tel.: +49-89-28923358; Fax: +49-8161-714753
E-mail address: homa.ghasemifard@wzw.tum.de

isotope signature ($\delta^{13}C$) can be applied to study the contribution of the biosphere on carbon cycles in the atmosphere (Keeling *et al.*, 1989; Miller *et al.*, 2003).

Atmospheric CO_2 and $\delta^{13}C$ have been studied on both regional and global scales at different sites with various techniques (Levin *et al.*, 1995; Tuzson *et al.*, 2011; Sturm *et al.*, 2013; Moore and Jacobson, 2015; Xia *et al.*, 2015; Pang *et al.*, 2016a). For instance, Xia *et al.* (2015) analyzed measurements of atmospheric CO_2 concentration and its stable isotope ratios ($\delta^{13}C$) at the regional background station Lin'an (LAN) in China to identify the isotopic signature of CO_2 sinks and sources. They concluded that during the winter season (Dec–Feb) coal combustion is the major CO_2 source due to domestic heating. The relatively high isotopic signature (~21.32‰) of sources and sinks during the vegetation season (Mar–Nov) was attributed to the significant contribution of biological activities at LAN. Sturm *et al.* (2013) presented continuous measurements of atmospheric CO_2 isotopes ($\delta^{13}C$ and $\delta^{18}O$) at the High Altitude Research Station Jungfraujoch (JFJ), Switzerland. Based on the high temporal resolution of their measurements (e.g., in comparison to flask samples), diurnal and hourly variations could be analyzed. They determined that diurnal cycles of atmospheric CO_2 and its isotopic compositions were small; however, the day-to-day variability depending on the origin of the air masses arriving at JFJ was larger. Based on this, the footprint clustering by the backward Lagrangian particle dispersion model FLEXPART revealed different CO_2, $\delta^{13}C$, and $\delta^{18}O$ values depending on the origin of air masses and surface residence time. Moore and Jacobson (2015) differentiated sources of atmospheric CO_2 by records of CO_2 concentration and carbon isotope composition ($\delta^{13}C$) at Evanston, an urban site north of Chicago, the third largest city in the United States.

Measurements of CO_2 mixing ratios in combination with stable CO_2 isotopes in the atmosphere at high altitude (background) sites may provide valuable information on carbon source and sink mechanisms (Zhou *et al.*, 2006; Sturm *et al.*, 2013; Yuan *et al.*, 2018). The variability of the atmospheric CO_2 mixing ratio and $\delta^{13}C$ is related to the history of air masses arriving at a measurement site, such as whether the air traveled through the free troposphere or has been influenced by the planetary boundary layer (PBL). Therefore, many atmospheric studies have applied trajectory statistical methods to identify the sources and their contribution to mixing ratios. Fleming *et al.* (2012) reviewed more than 150 studies dealing with back trajectories, cluster analyses and residence time. However, most of them applied air-mass history to identify transport pathways and potential sources but not sink contributions. It is well known that the effect of biospherical activity as well as strong influences of thermal convection (local transport processes from the boundary layer) may complicate the study of atmospheric CO_2 and $\delta^{13}C$ (Zellweger *et al.*, 2003; Sturm *et al.*, 2013).

In the present study, we (1) describe the specific corrections and selections of the data recorded by a non-upgraded G1101-i analyzer, (2) analyze the diurnal and seasonal patterns of atmospheric CO_2 mixing ratios and $\delta^{13}C$ and (3) identify potential CO_2 source and sink locations with the help of backward trajectories and the potential source contribution function.

MATERIAL AND METHODS

Measurement Site

The Environmental Research Station Schneefernerhaus (UFS) is part of the Global Atmosphere Watch (GAW) Global Observatory Zugspitze/Hohenpeissenberg in Germany. It is located in the northern limestone Alps at the border of Germany and Austria (47°25′00″N, 10°58′46″E) about 90 km southwest of Munich. The UFS is situated at an altitude of 2650 m above sea level (a.s.l.) on the southern slope of Zugspitze mountain massif. It can receive representative free tropospheric air but is also influenced by polluted air masses from the planetary boundary layer (PBL), especially during the day and in summer (Zellweger *et al.*, 2003; Pandey Deolal *et al.*, 2014; Leuchner *et al.*, 2016). Due to its location on a southern slope, northerly winds are mostly blocked (see Fig. 1) while there is wind channeling of western and eastern winds by the west side of the mountain ridge and the Rein Valley, respectively (Gantner *et al.*, 2003; Risius *et al.*, 2015). Due to diverse and intensive human activities in the vicinity of the UFS, from skiing and hiking areas as well as associated tourist services, the GAW site is categorized as a "weakly influenced, constant deposition" site (Henne *et al.*, 2010; Ferrarese *et al.*, 2015). Further detailed information can be found in the UFS station information system (http://www.schneefernerhaus.de/en/home.html).

Instrumentation

A wavelength-scanned cavity ring down spectrometer (G1101-i, Picarro Inc. USA) was installed in the laboratory on the 4th floor of the UFS building. It was operated from May 2012 to November 2014 (except for a downtime period in May and June 2013 due to a pump defect and its subsequent replacement). CO_2 mixing ratios and $\delta^{13}C$ were measured at a rate of 0.1 Hz. The air inlet for the instrument was located on a terrace above the laboratory roof at an altitude of 2670 m a.s.l. The inlet cap was constantly heated to prevent ice formation. The inner part of the inlet tube was made of borosilicate glass and was constantly regulated to a low positive temperature of ca. 5°C to avoid water condensation. The inlet tube (length: 3.5 m) was connected to a common manifold (glass, 4.2 m in length, 8 cm inner diameter) that was used for all measuring devices and species at the GAW station (Zellweger *et al.*, 2011). A 2 m 1/8″ stainless steel pipe connected the instrument to the inlet line, via a VICI (Valco Instruments Company Inc.) rotary valve that switched between ambient air and standard gases.

Isotopic ratio measurements of $^{13}C/^{12}C$ are expressed in per mil (‰), defined by the following Eq. (1) as:

$$\delta^{13}C = \left(\frac{\left(^{13}C / {}^{12}C\right)_{sample} - \left(^{13}C / {}^{12}C\right)_{standard}}{\left(^{13}C / {}^{12}C\right)_{standard}} \right) \times 1000 \qquad (1)$$

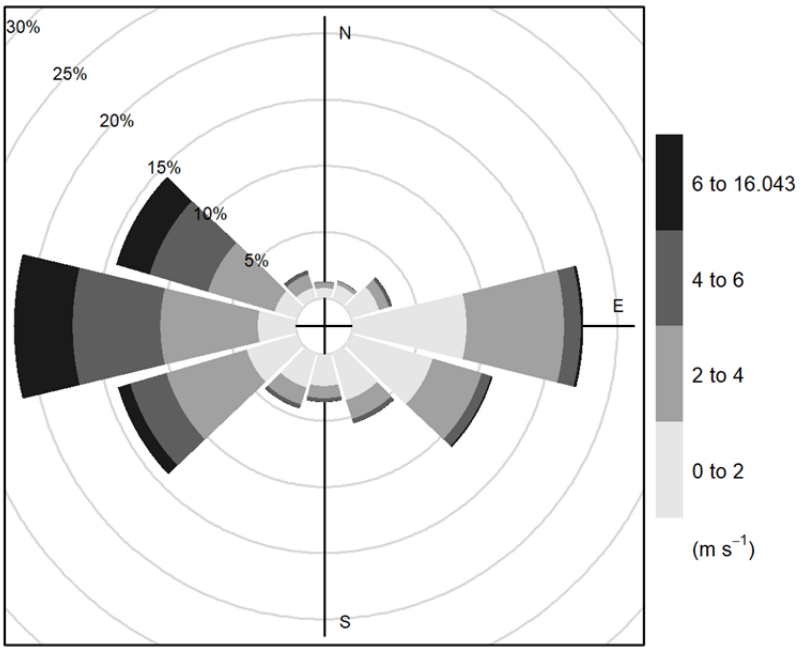

Fig. 1. Windrose at UFS, obtained from hourly wind data over the entire study period (May 2012–November 2014). Wind speed and direction are classified into colored segments; gray circles show the cumulated percentage of occurrence.

Isotopic values were given relative to the international standard VPDB-CO_2 (Vienna Pee Dee Belemnite) (Brand *et al.*, 2010). Measurements of CO_2 and $\delta^{13}C$ were calibrated using two working standard gases with high and low concentrations (DEUSTE Steininger GmbH) of the certified CO_2 mixing ratios and the isotopic compositions (Standard 1: 350.1 ± 0.50 ppm CO_2 mixing ratio and –3.28 ± 0.164‰ $\delta^{13}C$; Standard 2: 503.4 ± 0.50 ppm CO_2 mixing ratio and –20.03 ± 1.002‰ $\delta^{13}C$) in synthetic air. Each standard gas was fed into the analyzer for one hour every 7 days using an open-split configuration. After the data collection period, both gas standards were reanalyzed at the laboratory of the Max Planck Institute for Biogeochemistry (MPI-BGC), Jena, Germany, in order to confirm the quality of the calibration and the stability of the standards. The measured $\delta^{13}C$ values (Standard 1: –3.19 ± 0.009‰ $\delta^{13}C$; Standard 2: –20.26 ± 0.01‰ $\delta^{13}C$) agreed well with the original values within the given range of GAW data quality objectives (±0.01‰). The standard gases were also analyzed for other trace gas concentrations. Except for N_2O (Standard 1 and 2: 0.1 ppm) and CO (Standard 1: 6 ppb; Standard 2: 5.47 ppb), no other species (CH_4, H_2O, SF_6) could be detected.

The German Meteorological Service (Deutscher Wetterdienst, DWD) provided wind speed and wind direction data from the UFS in a one-minute time interval, and for this study, hourly averaged data are presented. In addition, we used CO_2 and CH_4 data measured with a Picarro Envirosense 3000i instrument to correct our measured data (see the section "Correction of CO_2"). This instrument, using cavity ring down spectroscopy, was operated by the German Environment Agency (Umweltbundesamt, UBA) connected to the same inlet as our Picarro G1101-i, therefore measured identical air sample, and was operated in the same air conditioned laboratory. For this device, water vapor in the ambient air was removed by cold traps. Gas mixtures for working standards of this device were equally delivered by DEUSTE Steininger GmbH, Germany. The station standards for interconnection with the international standard reference were reported on WMO X-2007 scale for CO_2 and WMO X2004a scale for CH_4 by NOAA, Boulder, Colorado, USA. Calibration and quality assurance for these atmospheric compounds followed the standard operating procedures of UBA in accordance with GAW quality standards. Since CO_2 measurements from UBA are reported to the WMO World Data Centre for Greenhouse Gases, the respective CO_2 data in the section "Correction of CO_2" will be referred to as CO_2 data of Global Atmosphere Watch ($CO_{2,\,GAW}$).

Optimal Integration Time and Precision

The Allan variance method (Allan, 1966; Werle *et al.*, 1993; Chen *et al.*, 2016) was applied to determine the optimal integration time for the measurements and to determine the best precision, using Standard 1 (CO_2: 350.1 ± 0.50 ppm; $\delta^{13}C$: –3.28 ± 0.164‰; Fig. 2). For this purpose, a long-term measurement of 24 h duration in February 2014 was analyzed. When integrating less than the optimum integration time, the Allan deviation follows a slope of –1/2 in the double logarithmic scale, indicating that white noise is dominating. When integrating beyond the optimum integration time, the Allan deviation rises and follows a slope of 1/2, indicating an instrument drift.

The optimum integration time minimizing the Allan deviation was around 1 hour for CO_2 and around 2 hours for $\delta^{13}C$. The best achievable precision (1 sigma) was 4 ppb for CO_2 and 0.2‰ for $\delta^{13}C$, respectively (see Fig. 2). However, we used a shorter integration time of 30 minutes for the ambient measurements, which gave a precision of

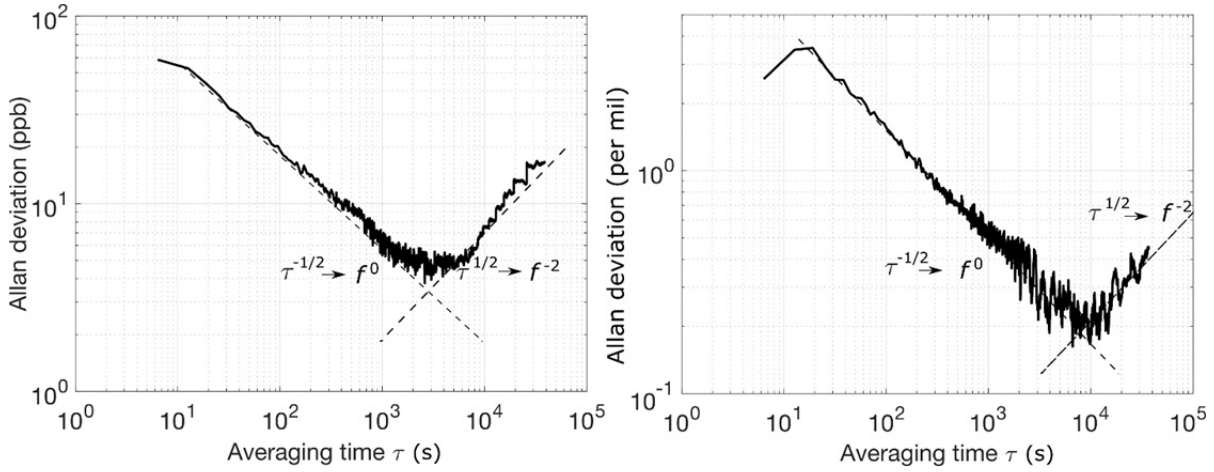

Fig. 2. Allan deviation plots for CO_2 (left) and $\delta^{13}C$ (right) as a function of the integrating time τ, based on a long-term measurement of Standard 1 (CO_2: 350.1 ± 0.50 ppm; $\delta^{13}C$: 3.28 ± 0.164‰). f stands for frequency and the black dashed lines represent slopes of –1/2 and 1/2, which correspond to power spectral densities S(f) = f^0 and S(f)= f^2, respectively. The Allan deviation follows a slope of –1/2 up to an integration time of 1 hour for CO_2 and of 2 hours for $\delta^{13}C$ and then turns over to a slope of 1/2 which defines a drift.

0.4‰ for $\delta^{13}C$ and 5–6 ppb for CO_2. For the very same analyzer, Wen *et al.* (2013) found the best precision of 0.08‰ at 2000 s, Vogel *et al.* (2013) had a precision of 0.2‰ at 5 min averaging, and Pang *et al.* (2016b) achieved optimum values of 0.08, 0.15, and 0.10‰ at 7600, 1900, and 1900 s for three reference gases. The precision of all studies on Picarro G1101-i shows better precision than the specification provided by the manufacturer (0.3‰).

Data Calibration and Correction

The G1101-i analyzer in this study was manufactured in 2010 and not upgraded during the measurement period to minimize downtime. As an alternative to upgrading, Picarro Inc. recommended later removal of spectral interference caused by CH_4 that can bias $\delta^{13}C$ by 0.4‰ ppm^{-1} (Vogel *et al.*, 2013) as well as water interferences. The latter include water vapor dilution, water vapor pressure broadening, and HDO spectral interference effects (Wen *et al.*, 2013). As we did not use any drying system and therefore measured the humid ambient gas, corrections for the dominating water vapor dilution effect were done according to Hoffnagle (2013); however, the smaller effects due to the water vapor pressure broadening and the HDO spectral interference effects were not corrected and their effects are about 2 ppm $\%v^{-1}$ water at 400 ppm of carbon dioxide, and up to 5‰ at ambient humidity (Nara *et al.*, 2012; Rella *et al.*, 2013; Wen *et al.*, 2013). According to Wen *et al.* (2013), even an upgrade of the analyzer would have led to overcorrections. The dependency of $\delta^{13}C$ on the CO_2 mixing ratio is of no concern to this study, as Vogel *et al.* (2013) showed that no dependency could be detected in the range of 303–437 ppm. Background gas concentrations and ratios (e.g., N_2/O_2 ratio and argon content) are known to influence the CRDS technology in general. While their natural variations usually generate negligible effects, large differences between ambient air and synthetic standards, such as the ones used in our study, may be problematic (Nara *et al.*, 2012; Rella *et al.*, 2013). However, no specific information or corrections are documented for the G1101-i analyzer.

Correction of $\delta^{13}C$

The isotopic analyzer reports the peak height of the near-infrared absorption spectrum for the rovibronic transition of $^{12}C^{16}O_2$ and $^{13}C^{16}O_2$ with arbitrary labeled $C12_{peak\text{-}BookAve}$ and $C13_{peak\text{-}BookAve}$, respectively. The ratio of the peak absorption values and the ratio of isotopic abundances are linear.

$$\delta\left(\frac{^{13}\mathrm{C}}{^{12}\mathrm{C}}\right)(\text{in permil}) = \mathrm{A}\left(\frac{C13_{peak-BookAve}}{C12_{peak-BookAve}}\right) + \mathrm{B} \quad (2)$$

A and B are instrument-specific constants and were provided by the manufacturer; they are the linear slope and intercept terms for computing the delta value from the ratio between $C13_{peak\text{-}BookAve}$ and $C12_{peak\text{-}BookAve}$ (Hoffnagle, 2013). The peak height can be affected by the absorption peaks for water, methane and other gases (Nara *et al.*, 2012; Rella *et al.*, 2013).

$\delta^{13}C$ ratios were corrected for methane and water vapor according to Hoffnagle (2013) using Eq. (3):

$$\delta^{13}C_{calculated} = A\times\left(\frac{C13_{peak-BookAve} - 0.003728\times \mathrm{CH_4}}{C12_{peak-BookAve}}\right) + B + \left(-2.98648648\times \mathrm{H_2O}\right) \quad (3)$$

H_2O is the water vapor concentration (in percent) and (–2.98648648 × H_2O) is the correction for the water interference. CH_4 is the methane concentration (in ppm), measured by the UBA device (Picarro Envirosense 3000i instrument).

Correction of CO_2

To quantify and correct water vapor effects on the CO_2 measurements, we compared the CO_2 mixing ratio for the wet gas stream measured by Picarro G1101-i analyzer ($CO_{2,meas}$) with CO_2 data of the accompanying instrument ($CO_{2,GAW}$). Although similar seasonal cycles were observed in Fig. 3, $CO_{2,\ meas}$ mixing ratios only showed a good agreement with $CO_{2,\ GAW}$ in wintertime when water vapor concentrations were low (0.39 ± 0.004%), while clear differences were observed in the summertime when water vapor concentrations were higher (1.81 ± 0.0048%). Wen *et al.* (2013) also measured a wet gas stream and compared the same analyzer as in this study with the Los Gatos DLT-100, observing that the mixing ratio measured by Picarro G1101-i was 2.2 ± 1.0 ppm lower than Los Gatos. They suggested that the water vapor dilution effect was partly responsible for this difference.

We corrected the dilution effect using ordinary least squares regression of the CO_2 mixing ratio difference between $CO_{2,GAW}$ and $CO_{2,\ meas}$. Concurrent with a pump failure and subsequent replacement (end of May/beginning of June 2013), the extent of the dilution effect changed and thus OLS regressions were carried out separately for the period before (Eq. (4)) and after (Eq. (5)) the pump failure, yielding

$$[CO_2]_{calculated} = 6.5[H_2O] - 2.7 + [CO_2]_{meas} \quad (4)$$

$$[CO_2]_{calculated} = 5.6[H_2O] - 0.85 + [CO_2]_{meas} \quad (5)$$

where $[H_2O]$ is water vapor concentration in percent, $[CO_2]_{meas}$ is CO_2 mixing ratio measured by our analyzer and $[CO_2]_{calculated}$ is the calculated and corrected mixing ratio. Fig. 4 illustrates the regressions before and after the pump failure. The physical reasons for the change in G1101-i behavior are not known and it seems unlikely that they were caused by the pump failure and replacement alone.

Corrected CO_2 data thus is in accordance with GAW data quality objectives (±0.1 ppm) (WMO, 2016). However, very small differences between the two analyzers (0.01 ± 0.42 and 0.02 ± 0.06 ppm before and after the pump replacement, respectively) remain and may be due to biases from spectral broadening and interferences (Rella, 2012).

Data Coverage and Selection

The temporal resolution of CRDS raw data should be in the order of seconds. In our case, however, the data periodically included measuring intervals far beyond the normal range (55 s and more). Since long measuring intervals are indicative of a slowed ring-down frequency and potential problems with the instrument (such as laser ageing or deficiencies in the optics, detector or data acquisition system), intervals > 55 s duration were removed from the dataset (personal communication by Dr. Renato Winkler, Picarro Inc.), which amounted to about 4.6% of data. The device returned to normal measuring intervals after restarts or laser readjustments. 1.8% of the data were missing due to the pump defect and replacement in May and June 2013. Another 3.8% of the data were missing due to the calibration procedures and/or power failures in the lab. At the end, this resulted in 89.8% of valid data over the entire measuring period.

The first 29 measurements of each calibration (ca. 3.5 minutes, less than 6% of each calibration) were discarded to ensure that no air sample from the previous measurement was left due to the transient response after valve switching (Vogel *et al.*, 2013). Then, from the remaining data, the average of each calibration was calculated. A smoothing spline was then fitted to all the averages to account for the residual variation in the calibration data and to fill a gap in the calibration measurements (8 months, July 2012–March 2013). This reduced the residual deviation between calibrated standard measurement and the real standard value from 0.05 ± 0.75‰ and 0.03 ± 0.53‰ (linear interpolation) to 0.0 ± 0.44‰ and 0.0 ± 0.32‰ (smoothing spline) for

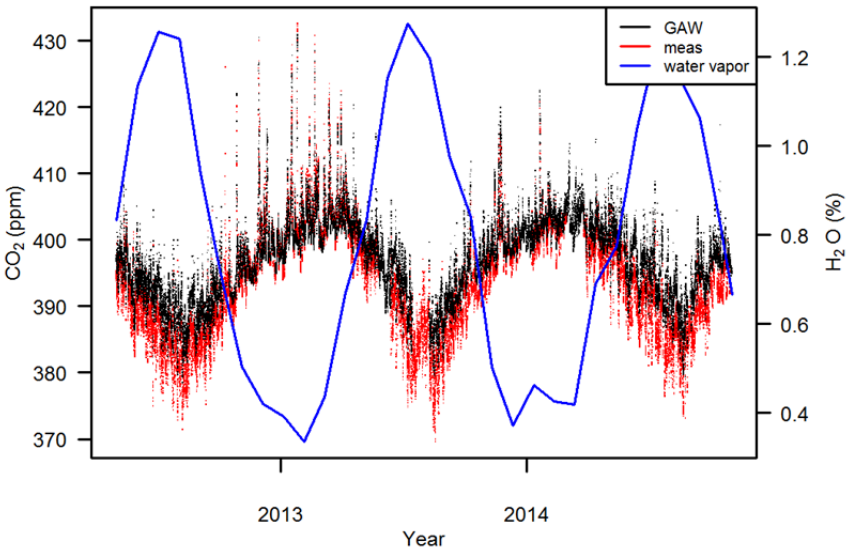

Fig. 3. Comparison of CO_2 mixing ratio measured by Picarro G1101-i (in red) without drying system to CO_2 measured by Picarro Envirosense 3000i (in black) dried by cold traps.

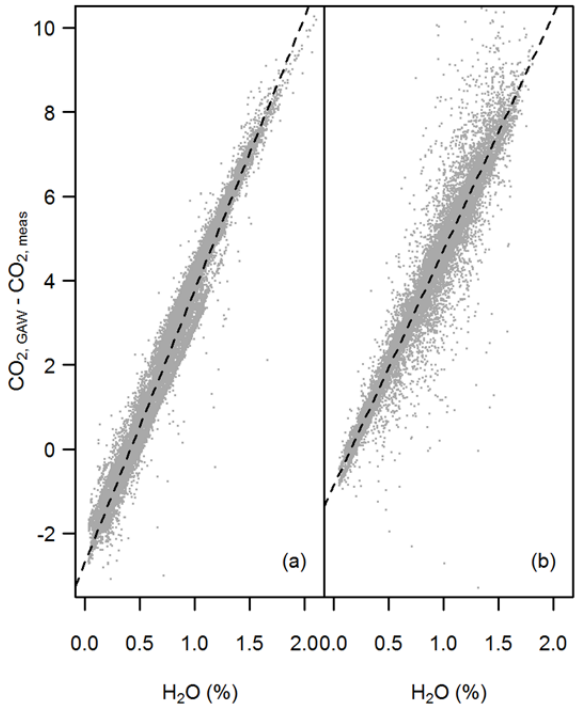

Fig. 4. Scatterplot of water vapor concentrations and difference of GAW and Picarro CO_2 measurements in the two phases before (a) and after (b) the pump replacement. The dashed line is an ordinary least squares regression line (coefficient of determination of linear regressions in (a): $R^2 = 0.97$, p-value < 0.001 and (b): $R^2 = 0.92$, p-value < 0.001).

Standards 1 and 2, respectively. Splines were calculated using the sm.spline function from the pspline package in R (Heckman and Ramsay, 1996). This function fitted a natural polynomial smoothing spline to the calibration values with 25 degree of freedom (out of 108 calibrations). Deviations between spline interpolated calibrations and the real standard values for each calibration are shown in Fig. 5. The smoothed coefficients were used for calibration. The two-point mixing ratio gain and offset calibration strategy of Bowling *et al.* (2003) was used for each measurement cycle as described above. Data were aggregated to 30-min averages by the statistical program *R* (R Core Team, 2016), which together with several packages was used for further analyses. At the end, uncertainty of calibration is estimated to be ±0.56 ppm for CO_2 and ±0.53‰ for $\delta^{13}C$ and combined measurement uncertainty is estimated to be ±0.56 ppm for CO_2 and ±0.56‰ for $\delta^{13}C$.

HYSPLIT Trajectory Model

One common method to establish source/sink-receptor relationships is to combine a calculated trajectory path of an air parcel with measured data at the time when the air parcel arrives at the site and consequently to determine locations of sources and sinks from these observations (Stohl, 1996).

In this work, the HYSPLIT (Hybrid Single-Particle Lagrangian Integrated Trajectory) Model was used to calculate backward trajectories to estimate air mass pathways to the UFS. Trajectories were calculated hourly for 96 h backward ending at UFS for the whole measurement period. The backward trajectory calculation was started at an altitude of 1500 m above ground level (a.g.l.) with respect to the model elevation at the coordinates of UFS, thus 3000 m a.s.l., roughly matching the real site altitude of 2650 m a.s.l. (UFS) and 2670 m a.s.l. (sample inlet).

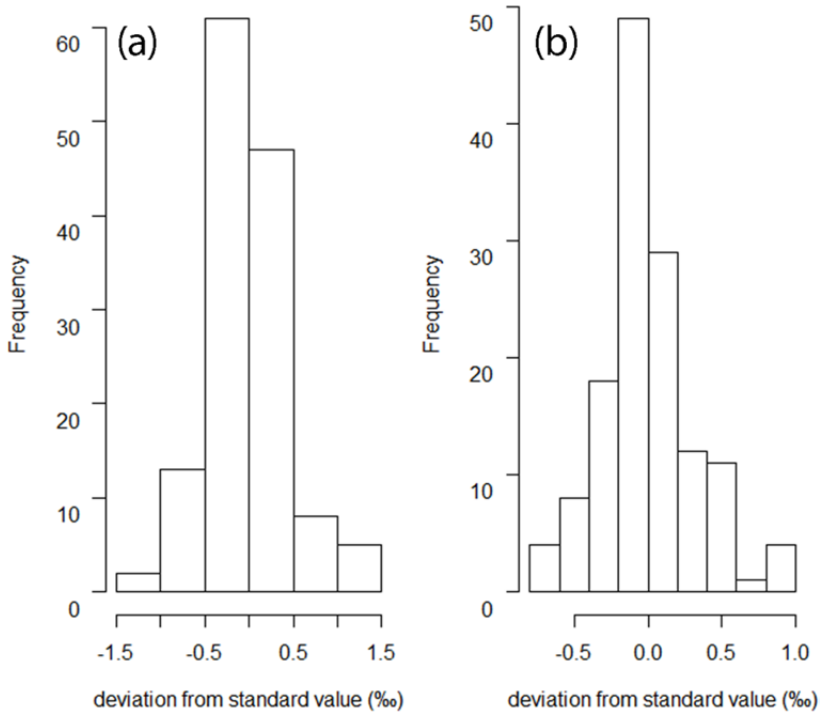

Fig. 5. Histogram of the deviation between spline and true standard value for (a) Standard 1 and (b) Standard 2.

The GFS (Global Forecast System) model "Grid 4" forecast weather data with 0.5° resolution was used as an underlying meteorological model. Forecasts from the 18:00 UTC cycle were obtained from the NOAA HAS data portal each day for the next 24 hours and were converted to ARL input model format. In case of the very few gaps (around 1.2%) in the GFS forecast data, forecasts from the previous day(s) were used as a replacement. For each trajectory time step, coordinates, altitude and mixing layer height (from the input model) were extracted. The backward trajectories were further processed by the openair package (Carslaw and Ropkins, 2012) within *R*. Here, clusters were calculated from all trajectories by applying an angle-based distance matrix method with the k-medoids algorithm (Sirois and Bottenheim, 1995). The number of clusters was set to five since for this number at least 10% of the trajectories were represented within each cluster. In order to filter the trajectories concerning their background air characteristics, they were split into two classes: (1) FT (free troposphere) trajectories when the trajectory height was higher than the mixing layer height for all time steps and (2) PBL influenced trajectories when the trajectory was below the calculated mixing layer height for at least one time step.

The potential source contribution function (PSCF) method using the residence time probability (Ashbaugh *et al.*, 1985; Seinfeld and Pandis, 2016) describes the spatial distribution of probable geographical source locations derived by trajectories. PSCF is defined as the probability that an air parcel with atmospheric component concentrations higher than a specific threshold arrives at the receptor site after having been observed to reside in a certain grid cell. The PSCF value (P_{ij}) for a given grid cell is then calculated as $P_{ij} = m_{ij}/n_{ij}$, in which n_{ij} is the total number of trajectory segment endpoints terminating within the grid cell(i,j) over the entire time of measurement and m_{ij} is the number of trajectory segment endpoints terminating within the grid cell(i,j) corresponding to trajectories associated with concentration values at the receptor site greater than a specific threshold (75th percentile of CO_2 and $\delta^{13}C$ in this study).

Robust Extraction of Baseline Signal

In order to calculate the long-term background values, the statistical method REBS (Robust Extraction of Baseline Signal) was applied, which is based on robust local regression (Ruckstuhl *et al.*, 2012). REBS is very flexible to derive the background levels of various trace gases at background measurement sites simultaneously (in our case both CO_2 and $\delta^{13}C$) due to its non-parametric basis. Sturm *et al.* (2013) used REBS for high alpine CO_2 and $\delta^{13}C$ measurements at Jungfraujoch, with results very similar to those obtained from the commonly applied data filtering method by Thoning *et al.* (1989). The background concentration was extracted using local regression (60 day windows) implemented in the rfbaseline function of the IDPmisc package (Locher and Ruckstuhl, 2012) in *R*. Missing data points were interpolated by a simple linear interpolation using the values from the hours before and after. The mean peak-to-peak seasonal amplitude was calculated from the background curves for an entire 2-year period (2012–2014).

Remote Sensing Data

In order to assess the vegetation properties, information on the vegetation type and activity in summer (June–August) were required. Therefore, we used remotely sensed phenological data based on MODIS Land Cover (LC) data and the Normalized Difference Vegetation Index (NDVI), respectively. The latest LC was issued in 2012 at 0.5° × 0.5° resolution (Friedl *et al.*, 2010; Channan *et al.*, 2014). More information can be found in the Global Land Cover Facility (http://glcf.umd.edu/data/lc/). The LC classes were aggregated to the ones shown and described in Fig. 11(b). NDVI is derived from multiple Advanced Very High Resolution Radiometer (AVHRR) measurements and is an indicator of the greenness of vegetation in each pixel of the satellite image. It ranges from –1.0 to +1.0. NDVI values below zero are excluded from this study because they indicate no vegetation, such as rock, sand or snow. Sparse vegetation such as grassland or cropland results in moderate NDVI values (0.2–0.5) and dense vegetation such as tropical forests results in high NDVI values (0.6–0.9). In this study, we averaged the respective NDVI values for the three months of summer (June to August) in the year 2012. The NDVI data were downloaded from the ECOCAST directory of the NASA Ames Ecological Forecasting Lab, version 3g.v0 (https://ecocast.arc.nasa.gov/data/pub/gimms/3g.v0/) for 2012.

RESULTS AND DISCUSSION

Atmospheric CO_2 and $\delta^{13}C$

Time series of CO_2 mixing ratios and $\delta^{13}C$ recorded from May 1, 2012, to Nov. 2, 2014, are displayed in Fig. 6. This includes both hourly data and fitted background concentrations, using the REBS technique. Fig. 6 shows a clear seasonal variation of hourly mean CO_2 mixing ratios and $\delta^{13}C$ values. CO_2 mixing ratios simultaneously increase as $\delta^{13}C$ values decrease, which is associated with seasonal vegetation activity. The mean peak-to-peak amplitudes are 15.5 ± 0.15 ppm for CO_2 and 1.97 ± 0.53‰ for $\delta^{13}C$. The minimum CO_2 mixing ratios, as well as the maximum $\delta^{13}C$ values, occurred in August due to (preferentially $^{12}CO_2$) CO_2 terrestrial uptake being dominated by the biosphere. The maximum in CO_2 mixing ratios occurred in March and the minimum in $\delta^{13}C$ values in February when respiration is dominating. In contrast, the peak-to-peak amplitudes of CO_2 mixing ratios and $\delta^{13}C$ at the High Altitude Research Station Jungfraujoch (JFJ) on the northern ridge of the Swiss Alps (46°32′53″N, 7°59′2″E, 3580 m a.s.l.) are 11.0 ppm for CO_2 and 0.60‰ for $\delta^{13}C$ (Sturm *et al.*, 2013). These differences in seasonal amplitudes between UFS and JFJ are most likely due to altitude since JFJ is located 930 m higher than UFS. Consequently, air masses at JFJ are much less impacted by PBL and mostly are from the lower free troposphere. Although amplitudes of CO_2 mixing ratios and $\delta^{13}C$ from these two sites were different, the minimum and the maximum of CO_2 mixing ratios and $\delta^{13}C$ were recorded nearly at the same time of the year.

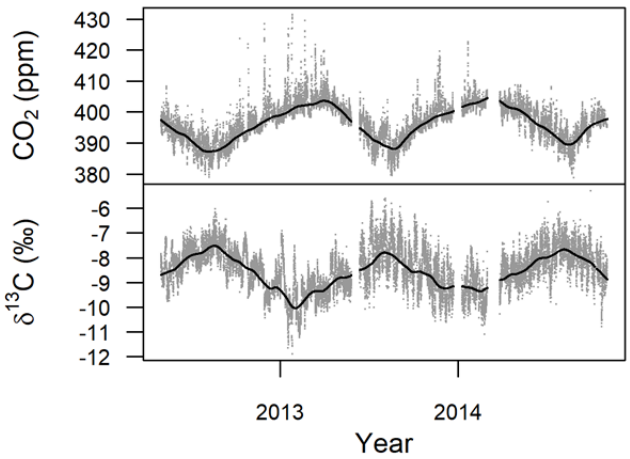

Fig. 6. Time series of hourly mean values of CO_2 and $\delta^{13}C$ for the period May 2012 to November 2014. Gray dots and solid lines represent the measurements and fitted background curves, respectively.

Diurnal Cycles

The mean diurnal cycles of CO_2 and $\delta^{13}C$ for each season are shown in Fig. 7. The CO_2 level started to increase at about 06:00 and reached the maxima around 09:00 to 10:00 during spring, summer, and autumn and at around 13:00 during winter, possibly due to local tourist activity, regional respiration, and regional anthropogenic emission potentially due to traffic. The daily peak-to-peak amplitude is 1.4 ppm in winter and 1.6 ppm in spring and autumn. The maximal diurnal change in CO_2 is found during summer months with a peak-to-peak amplitude of about 2.9 ppm. The strong afternoon drop during summer months is due to upward transport of PBL air from the valley. In summer, the CO_2 of the PBL air in lower levels is depleted due to photosynthetic uptake, indicating the influence of vegetation activity in the lower local and regional area around (below) the UFS. During summertime, the PBL influence at UFS has been identified for other parameters as well. Namely, the diurnal variation and high standard deviation of formaldehyde (HCHO) mixing ratio (Leuchner *et al.*, 2016) and the dependency of aerosol concentrations from the altitude of the mixing layer (Birmili *et al.*, 2009) could be detected. The mean diurnal cycle of $\delta^{13}C$ is very pronounced in summer with an amplitude of 0.4‰. The respective diurnal amplitudes in spring and autumn are 0.2‰ each, showing similar patterns as in summer. In contrast, winter months do not display any distinct diurnal cycles of $\delta^{13}C$.

For the Swiss site Jungfraujoch (JFJ), similar start of increase and maxima have been observed in spring, summer and autumn. However, amplitudes of diurnal variations in CO_2 mixing ratios and $\delta^{13}C$ were different (Sturm *et al.*, 2013). The diurnal peak-to-peak amplitude of CO_2 at JFJ

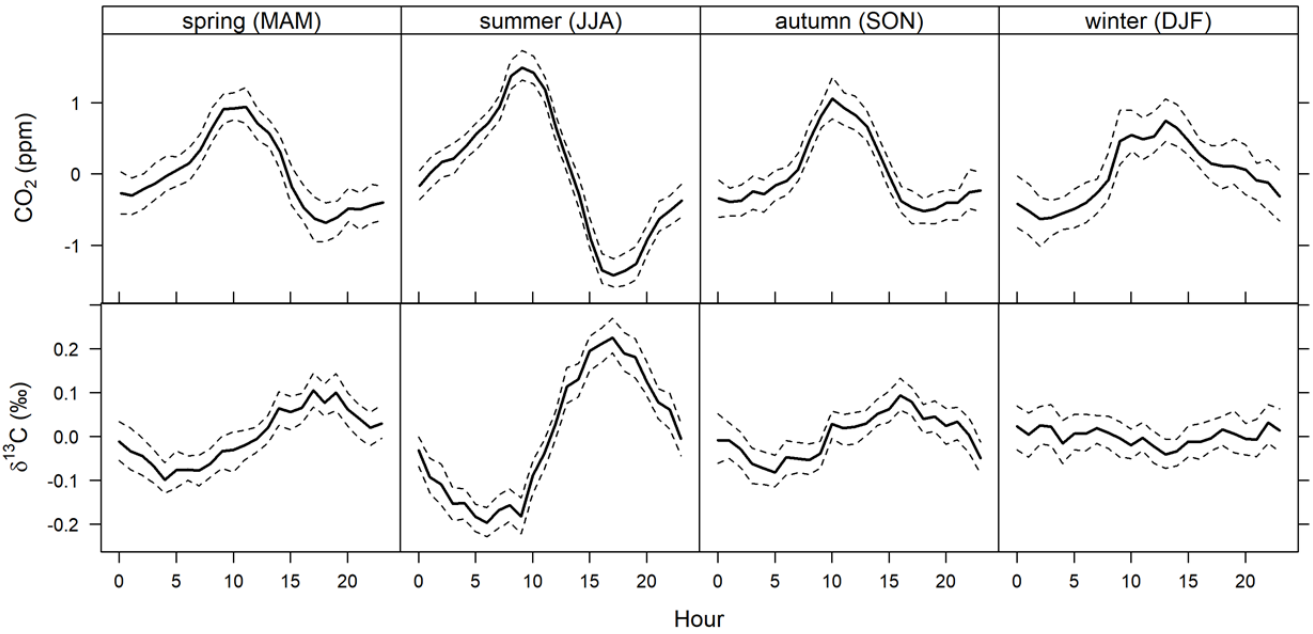

Fig. 7. Diurnal variations of the mean hourly CO_2 mixing ratios and $\delta^{13}C$ (solid line) relative to the respective daily means for the different seasons. Dashed lines show the 95% confidence intervals of the hourly mean calculated by bootstrap re-sampling.

in summer was 2 ppm (0.9 ppm less than at the UFS) and was 1 ppm in the other seasons (0.6 ppm less than at UFS in spring and autumn and 0.4 less in winter). In contrast to UFS, there were almost no diurnal variations of $\delta^{13}C$ at JFJ in spring, autumn and winter. In summer, JFJ exhibited a diurnal variation of about 0.3‰ less than at UFS with a comparable minimum in the morning and maximum in the afternoon. The larger amplitudes at UFS are likely due to a lower elevation (i.e., the station being closer to sinks and sources in the valley) and more tourist activity in the vicinity of UFS. Compared to urban sites, which are influenced much more strongly by local biogenic and anthropogenic activities, UFS shows much lower diurnal variability, e.g., by factors of 10 and 34 for $\delta^{13}C$ and CO_2, respectively, for a site in Kraków, Poland (Zimnoch *et al.*, 2004).

Back Trajectory Clusters

Characterization of the Clusters

The back trajectory analysis described in the section "HYSPLIT trajectory model" is shown in Fig. 8. Cluster 3 (C3) comprises the fastest and the most frequent (41.7%) flow at UFS and corresponds to a westerly flow from the mid-Atlantic Ocean. Cluster 4 is the second most abundant (19.5%), comprising flow from the northwest. Cluster 2 (14.9%) represents a moderately fast southwesterly flow. Slow-moving air masses coming from the central and west Mediterranean Basin are grouped in Cluster 1, representing 12.1% of the data. Cluster 5 corresponds to northeasterly flows and accounts for the smallest share (11.9%) of trajectories.

Variation of CO_2 Mixing Ratios and $\delta^{13}C$ among the Clusters

In order to study whether measured data of CO_2 and its isotopic composition systematically varied with air mass origin, we merged hourly CO_2 mixing ratios and $\delta^{13}C$ data with the respective trajectory information of the same time step (hourly) and grouped them into the five clusters described above (Fig. 8). Afterwards, data were filtered in two steps in order to separate the short-term deviations from the background concentrations and to derive clear information on potential background air masses. The background concentrations derived from the local regression were first subtracted from CO_2 and $\delta^{13}C$ values, providing ΔCO_2 and $\Delta\delta^{13}C$. Based on the 96-hour back trajectories of the HYSPLIT Model (see the section "HYSPLIT trajectory model"), the latter data were grouped into air masses in contact with PBL or of completely free troposphere origin. ΔCO_2 and $\Delta\delta^{13}C$ by trajectory clusters and seasons are shown in Fig. 9. The highest frequency of air masses contacting the PBL occurred in summer, with 21.3%, while the lowest frequency occurred in winter, with 10.3%. Spring and autumn had contact with the PBL in 14.6% and 12.6% of the cases, respectively.

In summer, CO_2 mixing ratios of clusters from the south significantly differed from the respective median of clusters from the north and west (significant levels of the Student's *t*-test are $p < 0.001$). In wintertime, the two clusters from the north (C4 and C5) showed the most pronounced differences in the measured ΔCO_2 and $\Delta\delta^{13}C$. Clusters 4 and 5 had the highest median ΔCO_2 values and, correspondingly, the lowest values in $\Delta\delta^{13}C$.

Using footprint clustering analysis for ΔCO_2 and $\Delta\delta^{13}C$ in wintertime for the JFJ site, Sturm *et al.* (2013) revealed that a cluster representing air masses with surface contact mostly over northern European land masses had the highest median ΔCO_2 value and the second lowest value in $\Delta\delta^{13}C$. Another cluster with high CO_2 mixing ratio had its origin in Eastern Europe. These two clusters according to residence time maps had the same direction as our C4 and C5 clusters, respectively. C4 was always associated with the lowest $\Delta\delta^{13}C$. This can be due to anthropogenic

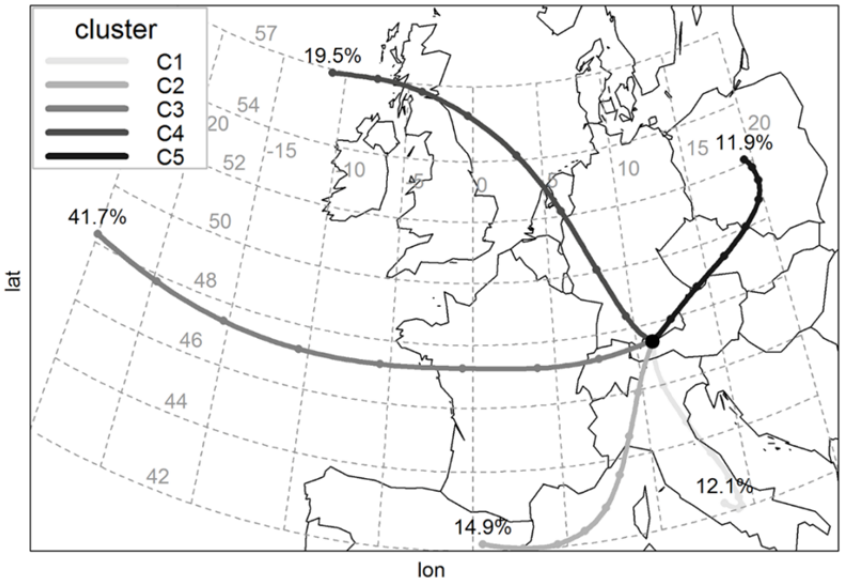

Fig. 8. Clustering of trajectories arriving at UFS in the entire period of May 2012 to November 2014 with their percentages of trajectories.

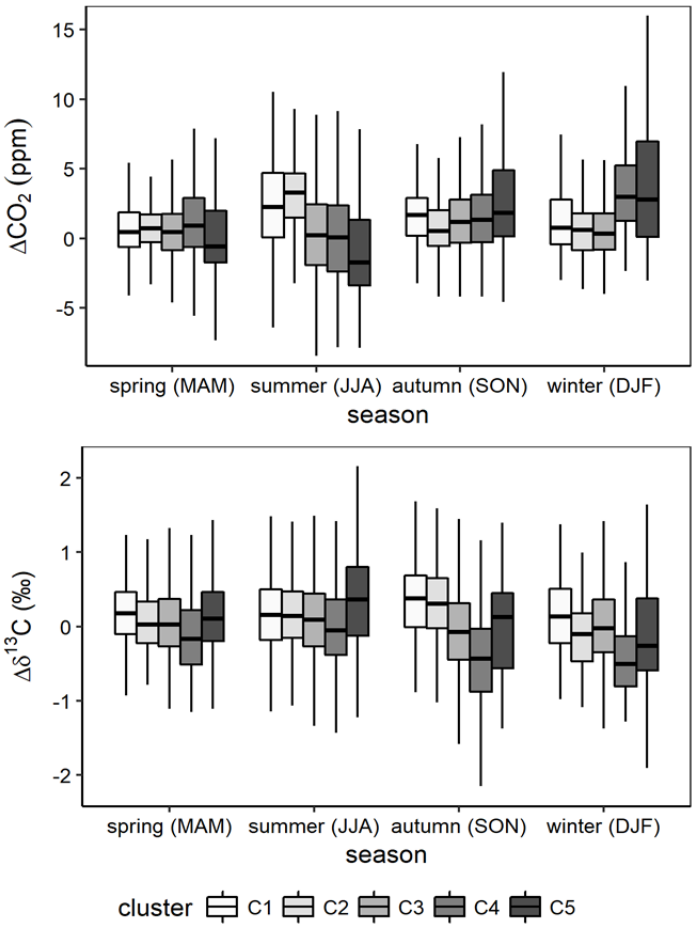

Fig. 9. Boxplots of ΔCO_2 mixing ratio and $\Delta\delta^{13}C$ for all seasons classified for the five clusters of Fig. 8 for the entire period. ΔCO_2 and $\Delta\delta^{13}C$ are filtered for free troposphere air and background concentrations are subtracted.

emissions from this direction (as shown in Fig. 10) being prevalent in all seasons. Cluster 3 had the least differences across seasons, both for ΔCO_2 and $\Delta\delta^{13}C$. In summer, C5 exhibited the highest $\Delta\delta^{13}C$ value and the lowest ΔCO_2 value, respectively.

Case Study: Combination of Trajectory Clusters and PSCF

The potential source contribution function (see the section "HYSPLIT trajectory model") was applied for the detection of geographical areas with an influence on the measured CO_2 concentration. This was done explicitly for air masses causing extremely high CO_2 concentrations (> 75th percentile) in Clusters 4 and 5. PSCF maps (Fig. 10) depict that the air masses from C5 can be traced back to the anthropogenic emissions from coal mining areas in Lusatia and from coal districts in East Germany, while air masses from C4 originate from northwestern Europe, including the high emission regions in the Netherlands and the German Ruhr area.

A comparable PSCF map for $\Delta\delta^{13}C$ (> 75th percentile), equally inferred by trajectories, describes the spatial distribution of probable geographical source locations for $\delta^{13}C$ (i.e., sinks of CO_2) in summer (Fig. 11). The combination of this PSCF map with MODIS land cover (LC) and NDVI map improve our understanding of the influences of air origin on seasonal variations in CO_2 and$\delta^{13}C$. Fig. 11 clearly illustrates that high values of $\Delta\delta^{13}C$ are influenced by Western, Central, and Southwestern Poland, which according to LC are predominantly croplands. Fig. 11(c) displays that this area is characterized by NDVI values greater than 0.6, indicating dense vegetation in these area with CO_2 uptake.

CONCLUSIONS

We presented a 2.5-year measurement time series of CO_2 mixing ratios and $\delta^{13}C$ at the high altitude GAW station UFS on the northern Alpine ridge. Since the Picarro G1101-i instrument was not upgraded to account for water vapor and methane interferences, comprehensive external data corrections and selections had to be implemented. These corrections would not have been feasible had there not been access to parallel measured carbon dioxide, methane and water vapor. Therefore, from the knowledge obtained with CO_2 measurement devices, adding a reliable drying system on the sample inlet line is strongly recommended.

Clear seasonalities in both the CO_2 mixing ratios and $\delta^{13}C$ were derived with seasonal amplitudes of 15.5 ± 0.15 ppm for CO_2 and of 1.97 ± 0.53‰ for $\delta^{13}C$. Seasonal and diurnal variations of both variables showed similar

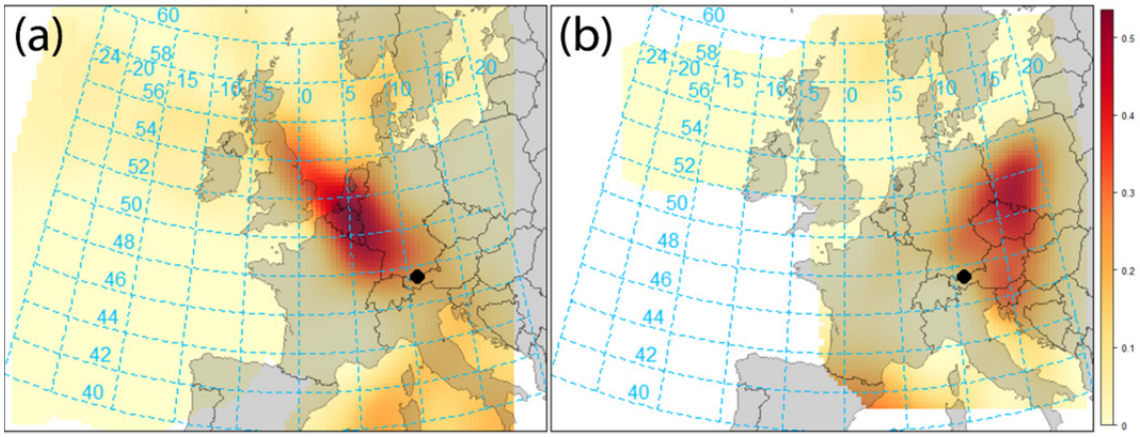

Fig. 10. Potential source contribution function plot for ΔCO_2 in wintertime (December to February). (a) PSCF map of Cluster 4 (NW) and (b) PSCF map of Cluster 5 (NE). The position of the site is shown by black circles.

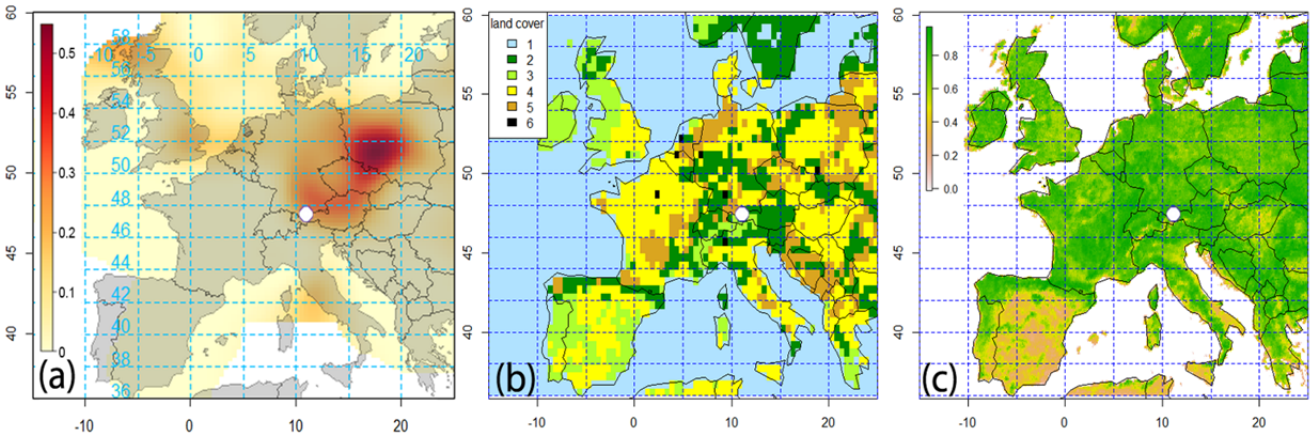

Fig. 11. (a) Potential source contribution function plot for $\Delta\delta^{13}C$ in the summertime (June to August) and (b) MODIS Land Cover for the year 2012. Land cover types on this map are grouped and labeled as follow: 1: water; 2: evergreen, deciduous as well as mixed forests; 3: closed and open shrublands, woody savannas, savannas, grassland; 4: croplands; 5: cropland/natural vegetation mosaic and 6: urban and build-up, (c) NDVI map. The position of the UFS site is shown by white circles.

patterns as at the High Altitude Research Station Jungfraujoch. However, the higher altitude of JFJ led to receiving more frequent free troposphere air masses, and therefore, amplitudes at UFS were generally larger than at JFJ in all seasons. The most pronounced diurnal variabilities were seen in summer at both sites, with an amplitude of 2.9 ppm and 2 ppm for the CO_2 mixing ratio at UFS and JFJ, respectively, and of 0.4‰ and 0.1‰ for the $\delta^{13}C$ at UFS and JFJ, respectively. The smallest diurnal variabilities occurred in winter, when the peak-to-peak amplitude was 1.4 ppm and 1 ppm for the CO_2 at UFS and JFJ and there was no discernible cycle for $\delta^{13}C$.

HYSPLIT classification of the air mass origins at UFS indicated predominant air masses from the west (41.2%), followed by the northwest (19.7%), southwest (14.8%), southeast (12.5%) and northeast (11.8%). The potential source contribution function, using back trajectories as well as atmospheric measurements, provided helpful indications of the origins of air masses potentially influencing a measuring station. So far, this method has been restricted to the identification of sources in air pollution studies (Begum *et al.*, 2005; Pekney *et al.*, 2006; Kaiser *et al.*, 2007; Pongkiatkul and Oanh, 2007; Zhu *et al.*, 2011), as the probability function in PSCF filters out concentrations below a(n) (arbitrary) threshold. However, in this study, $\delta^{13}C$ measurements and their inverse relationship to CO_2 allowed us to identify atmospheric CO_2 sinks. Among all clusters, high CO_2 mixing ratios in winter (anthropogenic sources) were associated with air masses originating in the Netherlands, the German Ruhr area and Lusatia, whereas high $\delta^{13}C$ values and low CO_2 mixing ratios in summer, representing a terrestrial biosphere sink influence, mostly originated in Poland. For an improved understanding of the contribution of the sources and sinks of carbon dioxide and the exchange of CO_2 between the terrestrial ecosystem and atmosphere, greenhouse gas emission models (e.g., the WRF Greenhouse Gas Model) can be used to simulate high-resolution transport of carbon dioxide.

Sinks and sources' isotopic signatures of continuously measured CO_2 (such as the data presented in this

publication) or records of distinct CO_2 variations (e.g., a sudden enhancement in atmospheric CO_2) could be further identified and quantified using the Keeling plot method (Keeling *et al.*, 1989; Vardag *et al.*, 2016). Access to other related tracers, e.g., carbon monoxide and radon-222 measured at the same site (as is done at UFS), may be a great help in this venture (Hirsch, 2007; Tuzson *et al.*, 2011).

ACKNOWLEDGMENTS

This study was funded by the Virtual Alpine Observatory project of the Bavarian State Ministry of the Environment and Consumer Protection. The authors would like to acknowledge Dr. Steven C. Wofsy and Maryann R. Sargent for fruitful discussions in data selection and correction, Rachel Chang, for her suggestions regarding source detections, and UFS staff for their kind support especially Dr. Rehm and Dr. Couret for essential help, including maintenances and technical supports, and UBA for the space in their lab and access to the facilities. The simulations of back trajectories were performed by Dr. Stephan Hachinger on the Compute Cloud of the Leibniz Supercomputing Centre (LRZ), Garching, Germany, and thanks for his important and valuable contribution to this research.

REFERENCES

Allan, D.W. (1966). Statistics of atomic frequency standards. *Proc. IEEE* 54: 221–230.

Ashbaugh, L.L., Malm, W.C. and Sadeh, W.Z. (1985). A residence time probability analysis of sulfur concentrations at grand Canyon National Park. *Atmos. Environ.* 19: 1263–1270.

Begum, B.A., Kim, E., Jeong, C.H., Lee, D.W. and Hopke, P.K. (2005). Evaluation of the potential source contribution function using the 2002 Quebec forest fire episode. *Atmos. Environ.* 39: 3719–3724.

Birmili, W., Ries, L., Sohmer, R., Anastou, A., Sonntag, A., König, K. and Levin, I. (2009). Fine and ultrafine aerosol particles at the GAW station Schneefernerhaus/Zugspitze. *Gefahrstoffe - Reinhalt. Luft* 69: 31–35.

Bowling, D.R., Sargent, S.D., Tanner, B.D. and Ehleringer, J.R. (2003). Tunable diode laser absorption spectroscopy for stable isotope studies of ecosystem–Atmosphere CO_2 exchange. *Agric. For. Meteorol.* 118: 1–19.

Brand, W.A., Assonov, S.S. and Coplen, T.B. (2010). Correction for the ^{17}O interference in $\delta(^{13}C)$ measurements when analyzing CO_2 with stable isotope mass spectrometry (IUPAC Technical Report). *Pure Appl. Chem.* 82: 1719–1733.

Carslaw, D.C. and Ropkins, K. (2012). openair — An R package for air quality data analysis. *Environ. Modell. Software* 27: 52–61.

Channan, S., Collins, K. and Emanuel, W. (2014). Global mosaics of the standard MODIS land cover type data. University of Maryland and the Pacific Northwest National Laboratory, College Park, Maryland, USA.

Chen, H., Winderlich, J., Gerbig, C., Hoefer, A., Rella, C., Crosson, E., Van Pelt, A., Steinbach, J., Kolle, O. and Beck, V. (2010). High-accuracy continuous airborne measurements of greenhouse gases (CO_2 and CH_4) using the cavity ring-down spectroscopy (CRDS) technique. *Atmos. Meas. Tech*. 3: 375–386.

Chen, J., Viatte, C., Hedelius, J.K., Jones, T., Franklin, J.E., Parker, H., Gottlieb, E.W., Wennberg, P.O., Dubey, M.K. and Wofsy, S.C. (2016). Differential column measurements using compact solar-tracking spectrometers. *Atmos. Chem. Phys.* 16: 8479.

Ciais, P., Sabine, C., Bala, G., Bopp, L., Brovkin, V., Canadell, J., Chhabra, A., DeFries, R., Galloway, J., Heimann, M., Jones, C., Le Quéré, C., Myneni, R.B., Piao, S. and Thornton, P. (2013). Carbon and Other Biogeochemical Cycles. In *Climate change 2013: The physical science basis. Contribution of working Group I to the fifth assessment report of the intergovernmental panel on climate change.* Stocker, T.F., Qin, D., Plattner, G.K., Tignor, M., Allen, S.K., Boschung, J., Nauels, A., Xia, Y., Bex, V. and Midgley, P.M. (Eds.). Cambridge University Press, Cambridge, United Kingdom and New York, NY, USA, pp. 465–570.

Cramer, W., Bondeau, A., Woodward, F.I., Prentice, I.C., Betts, R.A., Brovkin, V., Cox, P.., Fisher, V., Foley, J.A., Friend, A.D., Kucharik, C., Lomas, M.R., Ramankutty, N., Sitch, S., Smith, B., White, A. and Young-Molling, C. (2001). Global response of terrestrial ecosystem structure and function to CO_2 and climate change: Results from six dynamic global vegetation models. *Global Change Biol.* 7: 357–373.

Farquhar, G.D., Ehleringer, J.R. and Hubick, K.T. (1989). Carbon isotope discrimination and photosynthesis. *Annu. Rev. Plant Biol.* 40: 503–537.

Ferrarese, S., Apadula, F., Bertiglia, F., Cassardo, C., Ferrero, A., Fialdini, L., Francone, C., Heltai, D., Lanza, A. and Longhetto, A. (2015). Inspection of high–concentration CO_2 events at the Plateau Rosa Alpine station. *Atmos. Pollut. Res.* 6: 415–427.

Fleming, Z.L., Monks, P.S. and Manning, A.J. (2012). Untangling the influence of air-mass history in interpreting observed atmospheric composition. *Atmos. Res.* 104: 1–39.

Friedl, M.A., Sulla-Menashe, D., Tan, B., Schneider, A., Ramankutty, N., Sibley, A. and Huang, X. (2010). MODIS Collection 5 global land cover: Algorithm refinements and characterization of new datasets. *Remote Sens. Environ.* 114: 168–182.

Gantner, L., Hornsteiner, M., Egger, J. and Hartjenstein, G. (2003). The diurnal circulation of zugspitzplatt: Observations and modeling. *Meteorol. Z.* 12: 95–102.

Heckman, N. and Ramsay, J.O. (1996). Spline smoothing with model-based penalties. McGill University, unpublished manuscript.

Henne, S., Brunner, D., Folini, D., Solberg, S., Klausen, J. and Buchmann, B. (2010). Assessment of Parameters describing representativeness of air quality in-situ measurement sites. *Atmos. Chem. Phys.* 10: 3561–3581.

Hirsch, A. (2007). On using radon-222 and CO_2 to calculate regional-scale CO_2 fluxes. *Atmos. Chem. Phys.* 7: 3737–3747.

Hoffnagle, J. (2013). *Relationship between spectroscopic measurements and delta values reported by the G1101i isotopic carbon dioxide analyzers*. Picarro, Inc., Santa Clara, CA.

IPCC (2013). Annex II: Climate system scenario tables (Prather, M., Flato, G., Friedlingstein, P., Jones, C., Lamarque, J.F., Liao, H. andRasch, P. (Eds.)). In *Climate change 2013: The physical science basis. Contribution of working Group I to the fifth assessment report of the intergovernmental panel on climate change.* Stocker, T.F., Qin, D., Plattner, G.K., Tignor, M., Allen, S.K., Boschung, J., Nauels, A., Xia, Y., Bex, V. and Midgley, P.M. (Eds.). Cambridge University Press, Cambridge, United Kingdom and New York, NY, USA, pp. 1395–1446.

IPCC (2014). *Climate change 2014: Synthesis report. Contribution of working group I, II and III to the fifth assessment report of the intergovernmental panel on climate change*. Core Writing Team, R.K. Pachauri and L.A. Meyer (Eds.), IPCC, Geneva, Switzerland, p. 151.

Kaiser, A., Scheifinger, H., Spangl, W., Weiss, A., Gilge, S., Fricke, W., Ries, L., Cemas, D. and Jesenovec, B. (2007). Transport of nitrogen oxides, carbon monoxide and ozone to the Alpine Global Atmosphere Watch stations Jungfraujoch (Switzerland), Zugspitze and Hohenpeissenberg (Germany), Sonnblick (Austria) and Mt. Krvavec (Slovenia). *Atmos. Environ.* 41: 9273–9287.

Keeling, C.D., Bacastow, R.B., Carter, A., Piper, S.C., Whorf, T.P., Heimann, M., Mook, W.G. and Roeloffzen, H. (1989). A three-dimensional model of atmospheric CO_2 transport based on observed winds: 1. Analysis of observational data. In *Aspects of climate variability in the pacific and the western Americas*, Peterson D.H. (Ed.), American Geophysical Union, Geophysical Monograph.

Keeling, C.D., Piper, S.C., Whorf, T.P. and Keeling, R.F. (2011). Evolution of natural and anthropogenic fluxes of atmospheric CO_2 from 1957 to 2003. *Tellus B* 63: 1–22.

Le Quéré, C., Andrew, R.M., Canadell, J.G., Sitch, S., Korsbakken, J.I., Peters, G.P., Manning, A.C., Boden, T.A., Tans, P.P. and Houghton, R.A. (2016). Global carbon budget 2016. *Earth Syst. Sci. Data* 8: 605–649.

Leuchner, M., Ghasemifard, H., Lüpke, M., Ries, L., Schunk, C. and Menzel, A. (2016). Seasonal and diurnal variation of formaldehyde and its meteorological drivers at the GAW site Zugspitze. *Aerosol Air Qual. Res.* 16: 801–815.

Levin, I., Graul, R. and Trivett, N.B. (1995). Long-term observations of atmospheric CO_2 and carbon isotopes at continental sites in Germany. *Tellus B* 47: 23–34.

Locher, R and Ruckstuhl, A. *et al.* (2012). IDPmisc: Utilities of Institute of Data Analyses and Process Design (www.idp.zhaw.ch). R package version 1.1.17. https://CRAN.R-project.org/package=IDPmisc

Miller, J.B., Tans, P.P., White, J.W., Conway, T.J. and Vaughn, B.W. (2003). The atmospheric signal of terrestrial carbon isotopic discrimination and its implication for partitioning carbon fluxes. *Tellus B* 55: 197–206.

Mook, W., Bommerson, J. and Staverman, W. (1974). Carbon isotope fractionation between dissolved bicarbonate and gaseous carbon dioxide. *Earth Planet. Sci. Lett.* 22: 169–176.

Moore, J. and Jacobson, A.D. (2015). Seasonally varying contributions to urban CO_2 in the Chicago, Illinois, USA Region: Insights from a high-resolution CO_2 concentration and $\delta^{13}C$ record. *Elem. Sci. Anth.* 3: 52.

Nara, H., Tanimoto, H., Tohjima, Y., Mukai, H., Nojiri, Y., Katsumata, K. and Ralla, C.W. (2012). Effect of air composition (N_2, O_2, Ar, and H_2O) on CO_2 and CH_4 measurement by wavelength-scanned cavity ring-down spectroscopy: Calibration and measurement strategy. *Atmos. Meas. Tech.* 5: 2689–2701.

Pandey Deolal, S., Henne, S., Ries, L., Gilge, S., Weers, U., Steinbacher, M., Staehelin, J. and Peter, T. (2014). Analysis of elevated springtime levels of Peroxyacetyl nitrate (PAN) at the high Alpine research sites Jungfraujoch and Zugspitze. *Atmos. Chem. Phys.* 14: 12553–12571.

Pang, J., Wen, X. and Sun, X. (2016a). Mixing ratio and carbon isotopic composition investigation of atmospheric CO_2 in Beijing, China. *Sci. Total Environ.* 539: 322–330.

Pang, J., Wen, X., Sun, X. and Hauang, K. (2016b). Intercomparison of two cavity ring-down spectroscopy analyzers for atmospheric $^{13}CO_2/^{12}CO_2$ measurement. *Atmos. Meas. Tech.* 9: 3879–3891.

Pekney, N.J., Davidson, C.I., Zhou, L. and Hopke, P.K. (2006). Application of PSCF and CPF to PMF-modeled sources of $PM_{2.5}$ in Pittsburgh. *Aerosol Sci. Technol.* 40: 952–961.

Pongkiatkul, P. and Oanh, N.T.K. (2007). Assessment of potential long-range transport of particulate air pollution using trajectory modeling and monitoring data. *Atmos. Res.* 85: 3–17.

R Core Team (2016). R: A language and environment for statistical computing. Vienna: R Foundation for statistical computing; 2013. R foundation for statistical computing.

Ramsay, J.O. and Heckman, N. (1996). *Some theory for L-spline smoothing*. CRM Proceedings and Lecture Notes 18: 371–380.

Rella, C. (2012). Accurate stable carbon isotope ratio measurements in humid gas streams using the Picarro $\delta_{13}CO_2$ G2101-i gas analyzer. White Paper of Picarro Inc.

Rella, C.W., Chen, H., Andrews, A.E., Filges, A., Gerbig, C., Hatakka, J., Karion, A., Miles, N.L., Richardson, S.J., Steinbacher, M., Sweeney, C., Wastine, B. and Zellweger, C. (2013). High accuracy measurements of dry mole fractions of carbon dioxide and methane in humid air. *Atmos. Meas. Tech.* 6: 837–860.

Risius, S., Xu, H., Di Lorenzo, F., Xi, H., Siebert, H., Shaw, R. and Bodenschatz, E. (2015). Schneefernerhaus as a mountain research station for clouds and turbulence. *Atmos. Meas. Tech.* 8: 3209–3218.

Ruckstuhl, A.F., Henne, S., Reimann, S., Steinbacher, M., Vollmer, M., O'Doherty, S., Buchmann, B. and Hueglin, C. (2012). Robust extraction of baseline signal of

atmospheric trace species using local regression. *Atmos. Meas. Tech.* 5: 2613–2624.

Seinfeld, J.H. and Pandis, S.N. (2016). *Atmospheric chemistry and physics: From air pollution to climate change*, Third ed. John Wiley & Sons.

Sirois, A. and Bottenheim, J.W. (1995). Use of backward trajectories to interpret the 5-year record of PAN and O_3 ambient air concentrations at Kejimkujik National Park, Nova Scotia. *J. Geophys. Res*. 100: 2867–2881.

Stohl, A. (1996). Trajectory statistics-A new method to establish source-receptor relationships of air pollutants and its application to the transport of particulate sulfate in Europe. *Atmos. Environ.* 30: 579–587.

Sturm, P., Tuzson, B., Henne, S. and Emmenegger, L. (2013). Tracking isotopic signatures of CO_2 at the high altitude site Jungfraujoch with laser spectroscopy: Analytical improvements and representative results. *Atmos. Meas. Tech.* 6: 1659–1671.

Thoning, K., Tans, P. and Komhyr, W. (1989). Atmospheric carbon dioxide at Mauna Loa Observatory: 2. Analysis of the NOAA GMCC data, 1974–1985. *J. Geophys. Res*. 94: 8549–8565.

Tuzson, B., Henne, S., Brunner, D., Steinbacher, M., Mohn, J., Buchmann, B. and Emmenegger, L. (2011). Continuous isotopic composition measurements of tropospheric CO_2 at Jungfraujoch (3580 m a.s.l.), Switzerland: Real-time observation of regional pollution events. *Atmos. Chem. Phys.* 11: 1685–1696.

Vardag, S.N., Hammer, S. and Levin, I. (2016). Evaluation of 4 years of continuous $\delta^{13}C$ (CO_2) data using a moving keeling plot method. *Biogeosciences* 13: 4237–4251.

Vogel, F., Huang, L., Ernst, D., Giroux, L., Racki, S. and Worthy, D. (2013). Evaluation of a cavity ring-down spectrometer for in situ observations of $^{13}CO_2$. *Atmos. Meas. Tech.* 6: 301.

Wen, X.F., Meng, Y., Zhang, X.Y., Sun, X.M. and Lee, X. (2013). Evaluating calibration strategies for isotope ratio infrared spectroscopy for atmospheric $^{13}CO_2/^{12}CO_2$ measurement. *Atmos. Meas. Tech.* 6: 1491–1501.

Werle, P., Mücke, R. and Slemr, F. (1993). The limits of signal averaging in atmospheric trace-gas monitoring by tunable diode-laser absorption spectroscopy (TDLAS). *Appl. Phys. B* 57: 131–139.

WMO (2016). 18th WMO/IAEA meeting on carbon dioxide, other greenhouse gases and related tracers measurement techniques (GGMT-2015), La Jolla, CA, USA, 13-17 September 2015, GAW Report No. 229, World Meteorological Organization, Geneva, Switzerland.

Xia, L., Zhou, L., Tans, P.P., Liu, L., Zhang, G., Wang, H. and Luan, T. (2015). Atmospheric CO_2 and Its $\delta^{13}C$ measurements from flask sampling at Lin'an regional background station in China. *Atmos. Environ.* 117: 220–226.

Xu, J., Lee, X., Xiao, W., Cao, C., Liu, S., Wen, X., Xu, J., Zhang, Z. and Zhao, J. (2017). Interpreting the $^{13}C/^{12}C$ ratio of carbon dioxide in an urban airshed in the Yangtze River Delta, China. *Atmos. Chem. Phys.* 17: 3385–3399.

Yuan, Y., Ries, L., Petermeier, H., Steinbacher, M., Gómez-Peláez, A.J., Leuenberger, M.C., Schumacher, M., Trickl, T., Couret, C. and Meinhardt, F. (2018). Adaptive selection of diurnal minimum variation: A statistical strategy to obtain representative atmospheric CO_2 data and its application to European elevated mountain stations. *Atmos. Meas. Tech.* 11: 1501–1514.

Zellweger, C., Forrer, J., Hofer, P., Nyeki, S., Schwarzenbach, B., Weingartner, E., Ammann, M. and Baltensperger, U. (2003). Partitioning of reactive nitrogen (NO_y) and dependence on meteorological conditions in the lower free troposphere. *Atmos. Chem. Phys.* 3: 779–796.

Zellweger, C., Steinbacher, M. and Buchmann, B. (2011). System and performance audit of surface ozone, methane, carbon dioxide, nitrous oxide and carbon monoxide at the global GAW station Zugspitze-Schneefernerhaus, Germany, June 2011.

Zhou, L., White, J.W., Conway, T.J., Mukai, H., MacClune, K., Zhang, X., Wen, Y. and Li, J. (2006). Long-term record of atmospheric CO_2 and stable isotopic ratios at Waliguan Observatory: Seasonally averaged 1991–2002 source/sink signals, and a comparison of 1998–2002 record to the 11 selected sites in the Northern Hemisphere. *Global Biogeochem. Cycles* 20: GB2001.

Zhu, L., Huang, X., Shi, H., Cai, X. and Song, Y. (2011). Transport pathways and potential sources of PM_{10} in Beijing. *Atmos. Environ.* 45: 594–604.

Zimnoch, M., Florkowski, T., Necki, J.M. and Neubert, R.E. (2004). Diurnal variability of $\delta^{13}C$ and $\delta^{18}O$ of atmospheric CO_2 in the urban atmosphere of Kraków, Poland. *Isot. Environ. Health Stud.* 40: 129–143.

Received for review, January 10, 2018
Revised, July 6, 2018
Accepted, July 10, 2018